



HNTs/SiO₂ dual-network aerogels with improved strength and thermal insulation

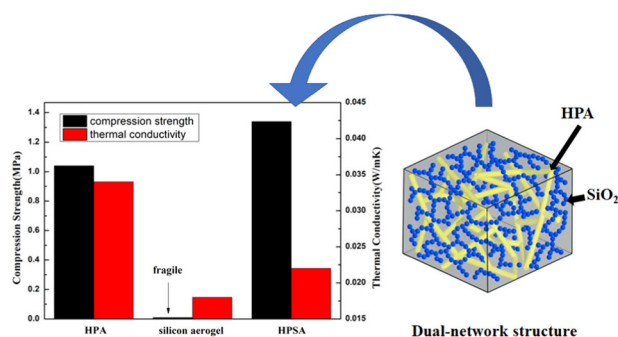
Hongli Liu¹ · Shixiong Li¹ · Hongyan Li¹ · Zhong Chen² · Jing Li¹ · Yajing Li¹

Received: 23 July 2018 / Accepted: 12 October 2018 / Published online: 23 October 2018
© Springer Science+Business Media, LLC, part of Springer Nature 2018

Abstract

Dual-network aerogels (HPSA) with improved mechanical property and thermal insulation were prepared by vacuum impregnation of HNTs/PVA aerogels (the first network aerogel, HPA) in tetraethoxysilane (TEOS). Scanning electron microscopy, transmission electron microscopy, energy dispersive spectroscopy, and N₂ adsorption–desorption analysis were used to study micromorphology and microstructure of HPSA, while compression tests and thermal conductivity tests were used to investigate related properties. The results showed that the dual-network frame was successfully constructed, this enabled HPSA to display enhanced compressive properties with increased HNTs content. The addition of silica sol improved the mesoporous characteristics including specific surface area and pore volume and also reduced the thermal conductivities. The first network made it possible for HPSA to possess good mechanical property, while SiO₂ aerogel allowed HPSA greater thermal insulation. The obtained aerogel samples exhibited a high compressive strength (i.e., 1.36 MPa) and a low thermal conductivity (i.e., 0.022 W/(m K)). HNTs/SiO₂ dual-network aerogels with improved strength and thermal insulation could show great potential in a wide variety of applications.

Graphical Abstract



Highlights

- Novel HNTs/SiO₂ dual-network aerogels were successfully prepared through cheap raw materials.
- The effects of HNTs content on the compressive strength and SiO₂ content on the thermal conductivity of aerogels were studied.
- The effects of dual-network frame on compressive strength and thermal conduction of aerogels were analyzed in detail by models.

✉ Hongli Liu
liuhongli@tcu.edu.cn

¹ School of Materials Science and Engineering, Tianjin Chengjian University, 26 Jinjing Road, Tianjin 300384, China

² School of Materials Science and Engineering, Nanyang Technological University, 50 Nanyang Avenue, Singapore 639798, Singapore

Keywords Dual-network aerogels · Halloysite nanotubes · Sol-gel · Compressive strength · Thermal conductivity

1 Introduction

Since the first report in 1931, aerogel has attracted extensive interests as a novel kind of nanoporous material [1, 2]. This material was usually made through a sol–gel chemical process and drying (supercritical or conventional drying) [3–5]. The invention of aerogels has greatly widened the path for developing novel materials due to their lots of unique properties (such as low densities, extremely low thermal conductivities, high acoustic resistance rates, high porosities, and high specific surface areas (SSA)), meriting consideration for a broad range of applications [6–11].

However, the use of silica aerogels for various practical applications has been limited mainly due to their inherent fragility [12–14]. Many researchers have made a lot of efforts and tried to overcome the disadvantages of poor mechanical performance. One of the most promising and convenient methods is the addition of fibers to the silica sol as supporting skeleton, resulting in the formation of fiber reinforced aerogel composites [15]. For instance, various fibers like ceramic [16, 17], mullite [18], glass [19], and aramid fibers [20] could be introduced to improve the mechanical properties of silica gels [15, 21]. These approaches led to an increase in strength by up to a factor of dozens of times but a decrease in thermal insulation performance [15, 21–25].

Halloysite nanotubes (HNTs), similar to kaolinite, are a type of natural aluminosilicate with nanotubular structure, and the chemical formula is generally expressed as $\text{Al}_2(\text{OH})_4\text{Si}_2\text{O}_5 \cdot n\text{H}_2\text{O}$ [26–30]. HNTs are widely deposited in China, Japan, Australia, Brazil, Belgium, and France. The rich deposits make it available in large amounts at low prices [28, 31]. HNTs have a range from 0.7 to 2 μm in length, while having a range from 40 to 60 nm in external diameter and 10 to 15 nm in internal diameter [27, 28, 30–34]. In contrast to many clay, HNTs consist of inside–outside alternate octahedral gibbsite $\text{Al}(\text{OH})_3$ and tetrahedral SiO_4 sheets in a 1:1 stoichiometric ratio [21, 26]. There are numerous applications due to the excellent characterization of HNTs such as electronic components, drug delivery, building field, cosmetics, and biomedical [27, 35–39]. According to previous reports, HNTs were evaluated as one-dimensional (1D) nanofillers for polymers. Many efforts have been devoted to the elaboration and study of mechanical and fire resistance properties of polymer/halloysite composites due to the environmentally friendly properties, low expense, good mechanical and thermal stability of HNTs [29, 40–42]. Li et al. [43] reported the PLLA/HNTs composite

nanofibers with improved mechanical strength had successfully been fabricated. He et al. [44] reported aerogels with polyvinyl alcohol (PVA) containing HNTs loaded with silica nanoparticle were prepared by sol–gel with freeze-drying technology, the compression strength of obtained aerogels greatly raised than that of as-received silica aerogel. Chu et al. [21] studied the mechanical strength and thermal conductivity of HNTs/silica composite aerogels, which were prepared via sol–gel method with the ambient-pressure drying process. The results proved the introduction of HNTs could effectively improve the mechanical performance of composites.

In this study, HNTs/ SiO_2 interpenetrating dual-network aerogels were successfully fabricated via vacuum impregnation and sol–gel processes by using HNTs, PVA, and tetraethoxysilane (TEOS) as raw materials. The micro-morphology and porous structure were characterized by scanning electron microscopy (SEM), transmission electron microscopy (TEM), and N_2 adsorption–desorption analysis. The elemental analysis was investigated by using energy dispersive spectroscopy (EDS). The compressive strength and thermal conductivities were measured by an electronic universal testing machine and thermal conductivity detector. The factors affecting compressive strength and heat conduction were studied by employing models.

2 Experimental section

2.1 Chemical reagents

PVA was supplied by Guangfu Fine Chemical Research Institute (Tianjin, China). HNTs were purchased from Fenghong Clay Chemical Co., Ltd. (Zhejiang, China). Deionized water, saturated borax solution, and TEOS were provided by Biotec Technology Development Co., Ltd. (Tianjin, China). Ethanol, HCl solution, and aqueous ammonia solution (NH_4OH) were provided by Jiangtian Uniform Technology Co., Ltd. (Tianjin, China). All reagents were used without further purification.

2.2 Preparation of HNTs/ SiO_2 dual-network aerogels

A 5.0 wt% PVA solution was prepared by dissolving 5 g of PVA in 95 ml deionized water at 80 °C under vigorous stirring for 3 h. 5 g HNTs were dispersed in 95 ml deionized water at 35 °C for 15 min to obtain a homogeneous suspension. PVA solution and HNTs suspension were mixed, then poured into a beaker and placed in an ultrasonic

disperser for 15 min. The mass ratios of HNTs suspension and PVA solution were $x:y$ with various x values of 14, 10, and 6 while y values of 6, 10, and 14. 0.5 g saturated borax solution was then added dropwise to the mixture by constant stirring until it became viscous and poured into a cylindrical mold having a diameter of 3 cm and a height of 4 cm. The mixture was allowed to freeze at $-25\text{ }^{\circ}\text{C}$ for 24 h, and then dried in a vacuum freeze drier for 48 h to obtain HNTs/PVA aerogel (the first network aerogel, HPA). The aerogel samples were labeled as $\text{H}_{14}\text{P}_6\text{A}$, $\text{H}_{10}\text{P}_{10}\text{A}$, and $\text{H}_6\text{P}_{14}\text{A}$ according to the mass ratios.

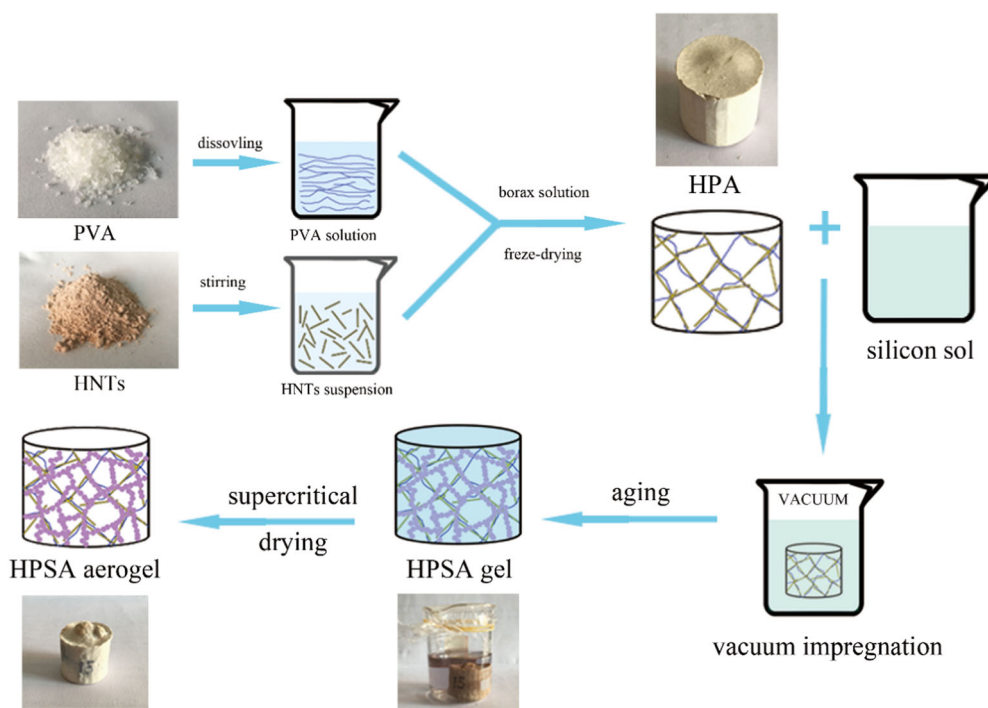
Table 1 Compositions of HPA and HPSA aerogels

Sample	Mass ratio		Molar ratio		
	HNTs	PVA	TEOS	H_2O	Ethanol
$\text{H}_6\text{P}_{14}\text{A}$	6	14	–	–	–
$\text{H}_{10}\text{P}_{10}\text{A}$	10	10	–	–	–
$\text{H}_{14}\text{P}_6\text{A}$	14	6	–	–	–
$\text{H}_6\text{P}_{14}\text{S}_{10}\text{A}$	6	14	1	5	20
$\text{H}_6\text{P}_{14}\text{S}_{15}\text{A}$	6	14	1	5	15
$\text{H}_6\text{P}_{14}\text{S}_{20}\text{A}$	6	14	1	5	10
$\text{H}_{10}\text{P}_{10}\text{S}_{10}\text{A}$	10	10	1	5	20
$\text{H}_{10}\text{P}_{10}\text{S}_{15}\text{A}$	10	10	1	5	15
$\text{H}_{10}\text{P}_{10}\text{S}_{20}\text{A}$	10	10	1	5	10
$\text{H}_{14}\text{P}_6\text{S}_{10}\text{A}$	14	6	1	5	20
$\text{H}_{14}\text{P}_6\text{S}_{15}\text{A}$	14	6	1	5	15
$\text{H}_{14}\text{P}_6\text{S}_{20}\text{A}$	14	6	1	5	10

TEOS , H_2O , and ethanol were added to a round bottom flask, stirred at $35\text{ }^{\circ}\text{C}$ for 10 min, then slowly dropped HCl solution with a concentration of 0.01 mol/L to adjust the pH to 2–3 and continue stirring for 20 min to obtain silica sol. The molar ratios of TEOS , H_2O , and ethanol were $1:5:z$ with various z values of 10, 15, and 20. The silica sol and HNTs/PVA aerogels were placed in a beaker under vacuum environment, and the HPA aerogels were immersed in silica sol. After air bubbles were completely removed, beaker was taken out and NH_4OH was added into the sol until $\text{pH} = 7$ and stirred to make the solution uniform. After 30 min, the sol became a wet gel and was then immersed in ethanol for 24 h at room temperature for further aging. The aged samples were loaded into a CO_2 supercritical drying kettle. The gels were supercritically dried at $45\text{ }^{\circ}\text{C}$ and 80 bar by slowly removing the supercritical fluid at a rate lower than 1 bar/min for 2 days to get dual-network aerogels (HPSA). The aerogels were labeled as HPS_{10}A , HPS_{15}A , and HPS_{20}A with various z values of 20, 15, and 10, respectively. Table 1 details the starting compositions of the resulting HPA and HPSA aerogels. The preparation process of the dual-network aerogels is shown in Scheme 1.

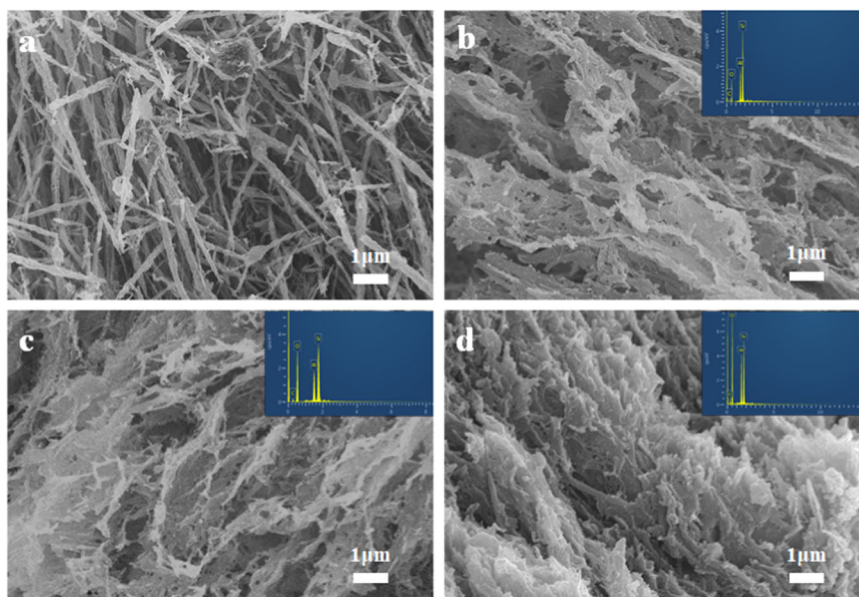
2.3 Characterization

The density of the aerogel (ρ) was calculated from the sample weight divided by its volume. The porosity was



Scheme 1 Preparation process of dual-network aerogel

Fig. 1 SEM images of **a** $H_{10}P_{10}A$; **b** $H_{10}P_{10}S_{10}A$; **c** $H_{10}P_{10}S_{15}A$; **d** $H_{10}P_{10}S_{20}A$



calculated according to Eq. (1):

$$\text{Porosity}(\%) = \left(1 - \frac{\rho}{\rho^*}\right) \times 100\% \quad (1)$$

$$\rho^* = 1.6(1 - w) + 2.1w \quad (2)$$

where ρ^* is the skeleton density of aerogels and w is the weight percent of silica in the aerogels. Here, the densities of HNTs and silica used in the calculation were 1.6 and 2.1 g cm^{-3} , respectively [2, 45, 46].

The morphological microstructure of the samples was characterized by SEM (JSM-7800F) at an acceleration voltage of 10 kV and TEM (JEOL 1011) at an acceleration voltage of 100 kV. The observed cross-section was prepared by mechanical force.

EDS analysis was applied to determine the composition of HPSA samples.

The SSA and pore size distribution of the aerogels were commonly measured by the multipoint Brunauer–Emmett–Teller (BET) and Barrett–Joyner–Halenda (BJH) methods on the basis of N_2 adsorption–desorption isotherms at 77 K with a 3H-2000PS1 analysis instrument.

Compression testing was conducted by using an electronic universal testing machine, fitted with a 15 kN load cell, at a crosshead of 1 mm min^{-1} . The dimension of all samples is about 40 mm in diameter and 30 mm in height.

The thermal conductivity was measured using a TC 3000E system, which has a cold–hot plate setup based on ASTM C 518 and ISO 8301. The transducer is integrating across an active area of 50 × 30 mm. The hot plate is set to 20 °C and the cold plate to 0 °C to measure the thermal conductivity across a mean temperature of 10 °C. The

thermal conductivity of each sample is an average of three times measurement.

3 Results and discussion

As shown in Fig. 1, the micromorphology of HPA and HPSA were investigated by SEM. The morphology of HPSA samples was altered as TEOS was dipped in. In Fig. 1a, HPA samples exhibit a typical porous structure with diameters of 1–2 μm . Interconnected HNTs are dispersed in the sample with uniform shapes and support the three-dimensional network. Figure 1b–d shows SEM images of $H_{10}P_{10}S_{10}A$, $H_{10}P_{10}S_{15}A$, and $H_{10}P_{10}S_{20}A$, respectively. Figure 1 shows that TEOS is successfully filled in the porous of HPA and are tightly connected with HNTs, indicating that both HNTs and solid silica nanoparticles are homogeneously distributed in the samples with similar size and this could be very helpful for improving the mechanical properties of silica aerogel (Fig. 6). Although the samples also retained a highly porous network structure, the HPSA had a much higher density than HPA due to the infiltration of silica sol between the pores (listed in Table 2). With the increase in silica content, the density raises from 0.0927 g cm^{-3} of $H_{10}P_{10}S_{10}A$ to 0.1217 g cm^{-3} of $H_{10}P_{10}S_{20}A$, while the porosity enhances from 91.42% to 93.24%, and these varieties would change the thermal conductivity of dual-network aerogels.

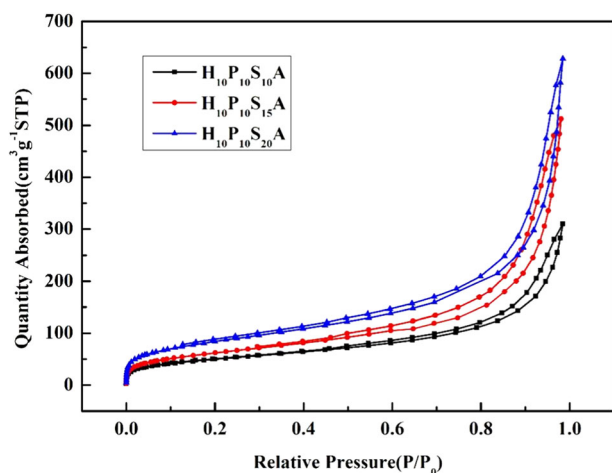
EDS analysis was performed to further confirm the immersion and distribution of silica in the HPSA. The EDS information was collected from HPSA samples. All the samples exhibit carbon, oxygen, and silicon signals, indicating that silica is distributed in HPA samples and the

Table 2 Porous characteristics of HPA and HPSA samples

Sample	Density (g cm ⁻³)	Porosity (%)	S _{BET} (m ² g ⁻¹)	Pore volume (cm ³ g ⁻¹)	Average pore size (nm)
H ₁₀ P ₁₀ A	0.0758	–	–	–	–
H ₁₀ P ₁₀ S ₁₀ A	0.0927	91.42	179	0.50	16.36
H ₁₀ P ₁₀ S ₁₅ A	0.1011	92.03	226	0.79	13.97
H ₁₀ P ₁₀ S ₂₀ A	0.1217	93.24	303	0.97	12.80

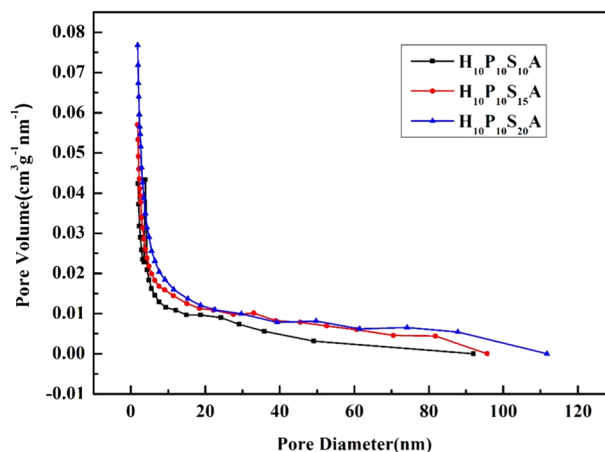
Table 3 Carbon, oxygen, and silicon content of different HPSA samples

Sample	C (wt%)	O (wt%)	Al (wt%)	Si (wt%)
H ₁₀ P ₁₀ S ₁₀ A	5.75	59.15	16.24	18.86
H ₁₀ P ₁₀ S ₁₅ A	4.06	61.05	14.56	20.33
H ₁₀ P ₁₀ S ₂₀ A	2.65	62.80	12.68	21.87

**Fig. 2** N₂ adsorption–desorption isotherms of HPSA

content of C, O, and Si elements are listed in Table 3. EDS analysis confirmed that HPSA contains largely distributed silica, could be reciprocally supported by the SEM, which is of great significance for the low thermal conductivity of the samples.

To further determine the microstructure of aerogels, BET gas sorptometry measurements were conducted to examine the porous nature of different HPSA samples. Figure 2 illustrates the N₂ adsorption–desorption isotherms. All of the isotherms of aerogels basically belong to type IV as defined by IUPAC, which was characteristic of mesoporous materials. The temporary locking of liquid N₂ and the delayed evaporation in the desorption isotherms indicated that the HPSA behaves similarly to the type H₃ hysteresis loops, implying the presence of hierarchical pores. The hysteresis loops which appear at lower relative pressure (0.4–0.8) indicated the presence of mesopores and that at higher relative pressure (0.8–1.0) was attributed to macropores [18, 21]. It was proposed that adsorption occurred on

**Fig. 3** Pore size distribution curves of HPSA

the surface of the silica aerogels and HNTs, which were overlaid with each other and constituted lots of pores contributing to the hysteresis loops. The sample as a whole exhibited the pore structure of silica aerogels, indicating that TEOS was well impregnated into the HPA samples and completely filled the pores. SSA of HPSA could be calculated by BET formula, and the SSA was 179, 226, and 303 m²/g, respectively (Table 2).

The pore size distribution, shown in Fig. 3, derived from the desorption branch and calculated from the isotherms using the BJH model, indicated that most of the pores fall into the size range of 2–50 nm and the average pore size is calculated to be 16.36, 13.97, and 12.80 nm, respectively (Table 2). It can be seen that the dual-network aerogels show a hierarchical porous structure, which was beneficial to prevent heat transfer (Fig. 7). The N₂ adsorption–desorption results were in good confirmation with the SEM observations. It can be seen that H₁₀P₁₀S₂₀A exhibited the smallest pore diameter much lower than that of H₁₀P₁₀S₁₀A. It could be that the more TEOS was added, which resulted in better cross-linking between silicon hydroxyls. This mesoporous structure was the main reason why the sample had good thermal insulation properties.

Figure 4a–d shows TEM images of H₁₀P₁₀A, H₁₀P₁₀S₁₀A, H₁₀P₁₀S₁₅A, and H₁₀P₁₀S₂₀A, respectively. Figure 4a shows a typical low-magnification TEM photograph of the H₁₀P₁₀A sample, in which HNTs about 600 nm in length and 50 nm in diameter overlapped with each other,

Fig. 4 TEM images of **a** $H_{10}P_{10}A$; **b** $H_{10}P_{10}S_{10}A$; **c** $H_{10}P_{10}S_{15}A$; **d** $H_{10}P_{10}S_{20}A$

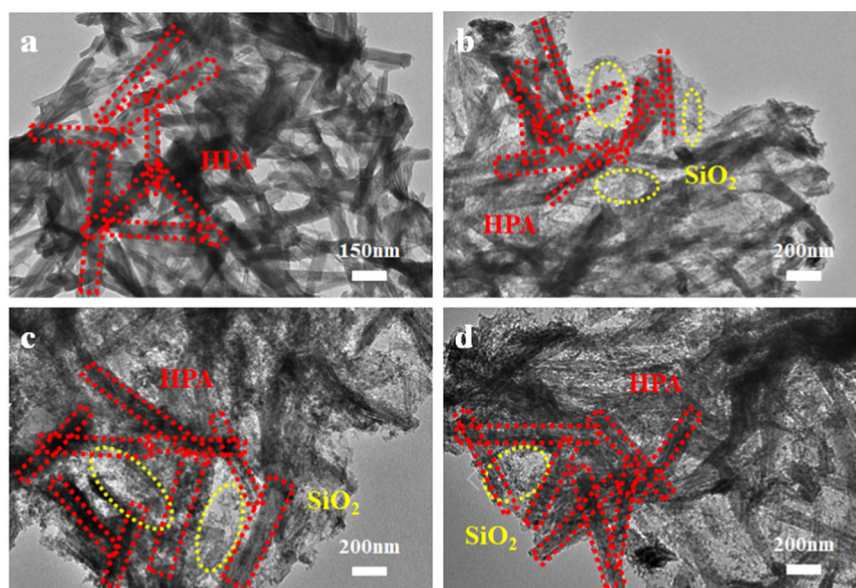


Fig. 5 Compressive strength test

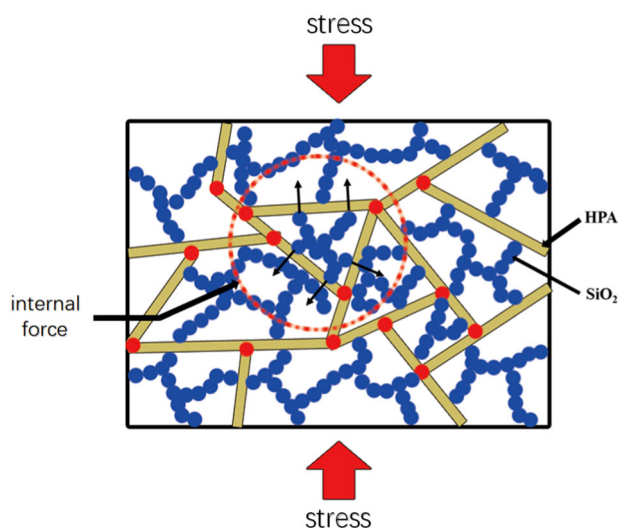


Fig. 6 Compressive strength modes of HPSA

Table 4 Compressive strength of different HPA and HPSA

Compressive strength (MPa)	Silica content		
	S ₁₀	S ₁₅	S ₂₀
$H_{10}P_{10}A$ (the first network)	1.04 ± 0.02	1.04 ± 0.02	1.04 ± 0.02
$H_6P_{14}SA$	1.15 ± 0.02	1.17 ± 0.02	1.19 ± 0.02
$H_{10}P_{10}SA$	1.30 ± 0.02	1.34 ± 0.02	1.36 ± 0.02
$H_{14}P_6SA$	1.43 ± 0.02	1.48 ± 0.02	1.51 ± 0.02

forming a 3-D network framework. Figure 4b–d displays uniform distribution of silica particles in HPA and the distance between the particles is less than 50 nm, suggesting that the materials mainly had a typical mesoporous structure as confirmed by N_2 adsorption–desorption analysis. As could be seen in Fig. 4, the dense distribution of nanoparticles indicated that the silica sol is completely immersed in HPA and filled the pores of samples. As the silica content increases, the nanoparticles become denser but the particle size does not change significantly, which leads to the decrease of the porosity and the increase of density. The results observed from TEM confirmed the conclusions in SEM and EDS.

Figure 5 is a photograph of HPSA sample subjected to compressive strength test on an electronic universal testing machine. In this study, compressive strength of HPSA sample could be expressed as σ_{HPSA} , while σ_{silica} of silica aerogel and σ_{HPA} of HPA. Benefiting from their intermolecular and nanoscaled structures (shown in Fig. 6), the HPSA aerogels exhibited enhanced compressive strength and σ_{HPSA} could be expressed as follows:

$$\sigma_{HPSA} > \sigma_{silica} + \sigma_{HPA} \quad (3)$$

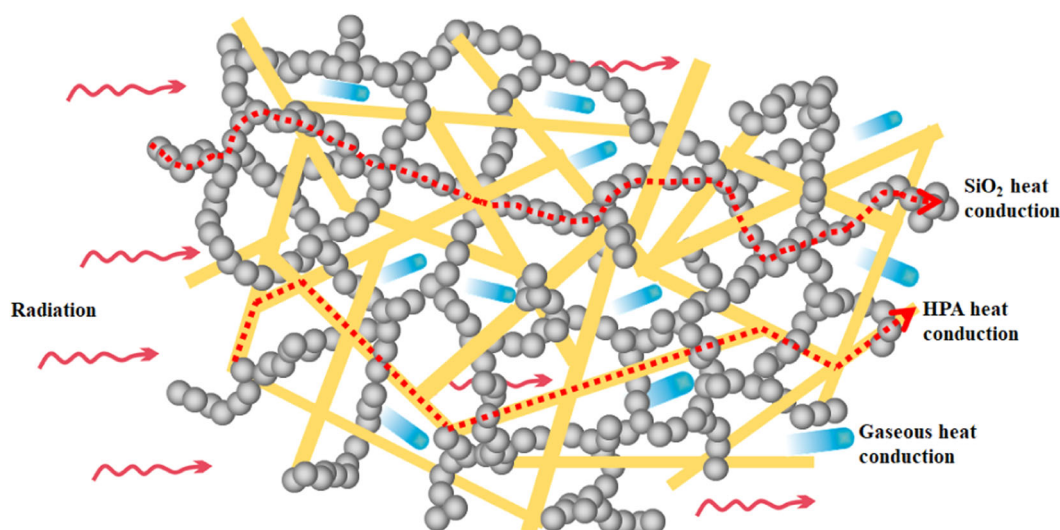


Fig. 7 Heat transfer mode within dual-network aerogel

where σ_{HPA} is much higher than σ_{silica} (the density and compression strength of silica aerogel are 0.09 g/cm^3 and $0.017\text{--}0.021 \text{ MPa}$ [47, 48]) attribute to nature excellent mechanical properties of HNTs, meanwhile, silica aerogel has merely strength because it is fragile. The internal force between silica particles and HPA is the reason why σ_{HPSA} is higher than the sum of σ_{silica} and σ_{HPA} , indicating that the halloysite skeleton could greatly enhance the silica aerogels' mechanical properties (Fig. 6). Table 4 displays that with the increase in the value of H:P, the compressive strength enhances significantly; with the increase of S value, the compressive strength of HPSA raises slightly. At H:P = 10:10, the sample has a compressive strength of 1.36 MPa, which is more than 30 times that of silica aerogel (the density is 0.09 g/cm^3) [47, 48]. HNTs/SiO₂ dual-network aerogels with promising compressive strength are of great help due to their applications in the field of building insulation.

In HPSA samples, effective thermal conductivity λ_e could be calculated by summing radiative thermal conductivities and gas–solid coupled heat conductivities according to Eqs. (4) and (5) [49, 50]:

$$\lambda_e = \lambda_r + \lambda_c \quad (4)$$

$$\lambda_e = \lambda_r + \lambda_g + \lambda_s \quad (5)$$

where λ_r is radiative thermal conductivity and λ_c is gas–solid coupled heat conductivity that depends on two heat transfer modes, namely, solid heat conduction (λ_s) and gas heat conduction (λ_g). Herein, we simplified the heat transfer model of HPSA, did not consider the thermal conduction among gas molecules and adjacent particles (such as quasi-lattice vibration) [51]. Figure 7 displays schematic of heat transfer modes within dual-network aerogel materials.

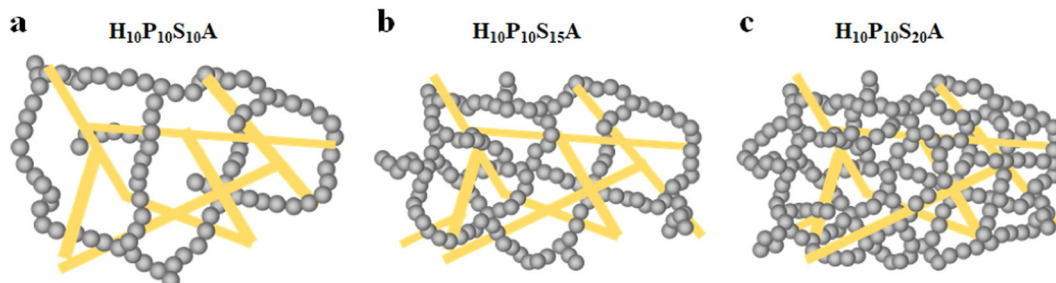
Considering effects of the two phases on microcosmic heat transfer, effective thermal conductivity can be decomposed into three parts in terms of physical means: contribution of radiative heat transfer λ_r , which is similar to radiative thermal conductivity, contributions of solid heat conduction λ_s , and gaseous heat conduction λ_g . Radiation thermal conduction could be neglected at room temperature, and in this study λ_s could be considered as two ways: solid conduction of HPA λ_{HPA} and solid conduction of silica aerogel λ_{silica} . Then, λ_e can be expressed as follows:

$$\lambda_e = \lambda_g + \lambda_{\text{HPA}} + \lambda_{\text{silica}} \quad (6)$$

The thermal conductivities of different HPSA samples are exhibited in Table 5. The difference between thermal conductivities indicate that with the increase in S value, the thermal conductivity of the sample begins to decrease first, but it would increase slightly after $S > 15$. This phenomenon could be explained by Fig. 8 (pictures from a to c are dual-network models of H₁₀P₁₀S₁₀A, H₁₀P₁₀S₁₅A, and H₁₀P₁₀S₂₀A, respectively), which illustrated the variation in λ_g , λ_{HPA} , and λ_{silica} under different silica content. Solid conduction of HPA λ_{HPA} remained nearly unchanged at a fixed ratio of H:P. Solid thermal conduction is improved, and gaseous thermal conduction declined with increasing silica. Thus, competition occurred between λ_{silica} and λ_g . λ_{silica} was predominant in heat transfer, and λ_{silica} would be influenced by the content of silica. In Fig. 8a, λ_g is higher than the others due to the larger pores, and $\lambda_{g(a)} > \lambda_{g(b)} > \lambda_{g(c)}$ while $\lambda_{\text{silica}(a)} < \lambda_{\text{silica}(b)} < \lambda_{\text{silica}(c)}$. In conclusion, the thermal conduction of dual-network aerogels is H₁₀P₁₀S₁₀A > H₁₀P₁₀S₂₀A > H₁₀P₁₀S₁₅A. In addition, with the decrease of H:M ratio, the thermal conductivity of HPSA shows a slight downward trend. This attributed to that HNTs heat conduction was better than PVA heat conduction.

Table 5 Thermal conductivity of different HPSA samples

Thermal conductivity (W/m K)	S ₁₀	S ₁₅	S ₂₀
H ₁₄ P ₆	0.027 ± 0.0005	0.023 ± 0.0005	0.024 ± 0.0005
H ₁₀ P ₁₀	0.026 ± 0.0005	0.022 ± 0.0005	0.023 ± 0.0005
H ₆ P ₁₄	0.025 ± 0.0005	0.022 ± 0.0005	0.023 ± 0.0005

**Fig. 8** Models of different dual-network aerogels

4 Conclusions

HNTs/SiO₂ dual-network aerogels (HPSA) with improved compressive strength and thermal insulation were prepared. The TEOS was well impregnated into the pore of HPA sample and formed an overall uniform dual-network mesoporous aerogel. The addition of HNTs greatly improved compressive strength compared with silica aerogel, while the addition of TEOS resulted in more homogeneous and great thermal insulation. N₂ adsorption–desorption test indicated that HPSA had a typical mesoporous structure, and HPSA samples had a SSA of 179.12–303.81 m² g⁻¹, a pore volume of 0.5060–0.9719 cm³ g⁻¹ and a pore size distribution of 12.80–16.36 nm. As the value of H:P ratio increased, the compressive strength of the HPSA sample raised moderately, with a compressive strength of HPSA up to 1.36 MPa at H:P = 10:10. As the TEOS increased, the thermal conductivity of HPSA showed a downward trend, and after decreased to a minimum value (HPS₁₅A), it began to rise. At Si = 15, HPSA sample had the lowest thermal conductivity (H₁₀P₁₀S₁₅A = 0.022 W/m K). This kind of aerogel with such properties could be promising for applications in building insulation, aerospace, chemical production, etc.

Acknowledgements This work was financially supported by the National Natural Science Foundation of China (Nos. 51772202 and 51472175).

Compliance with ethical standards

Conflict of interest The authors declare that they have no conflict of interest.

References

- Kistler S (1931) Coherent expanded aerogels and jellies. *Nature* 127:741
- Yuan B, Zhang JM, Mi QY, Yu J, Song R, Zhang J (2017) Transparent cellulose-silica composite aerogels with excellent flame retardancy via an in situ sol-gel process. *ACS Sustain Chem Eng* 5:11117–11123
- Amin S, Mohammad RS (2014) Improvements of reinforced silica aerogel nanocomposites thermal properties for architecture applications. *Int J Biol Macromol* 72:230–234
- Wei GS, Zhang YD, Xu C, Du XZ, Yang YP (2017) A thermal conductivity study of double-pore distributed powdered silica aerogels. *Int J Heat Mass Transfer* 108:1297–1304
- Hayase G, Kugimiya K, Ogawa M, Kodera Y, Kanamori K, Nakanishi K (2014) The thermal conductivity of polymethylsilsesquioxane aerogels and xerogels with varied pore sizes for practical application as thermal superinsulators. *J Mater Chem A* 2:6525–6531
- Zu GQ, Shen J, Zou LP, Wang WQ, Lian Y, Zhang ZH, Du A (2013) Nanoengineering super heat-resistant, strong alumina aerogels. *Chem Mater* 25:4757–4764
- Katsoulidis AP, He JQ, Katsoulidis MG (2012) Functional monolithic polymeric organic framework aerogel as reducing and hosting media for Ag nanoparticles and application in capturing of iodine vapors. *Chem Mater* 24:1937–1943
- Schiffres SN, Kim KH, Hu L, Mcgaughey AJH, Islam MF, Malen JA (2012) Gas diffusion, energy transport, and thermal accommodation in single-walled carbon nanotube aerogels. *Adv Funct Mater* 22:5251–5258
- Shang K, Yang JC, Cao ZJ, Liao W, Wang YZ, Schiraldi DA (2017) Novel polymer aerogel toward high dimensional stability, mechanical property, and fire safety. *ACS Appl Mater Interfaces* 9:22985–22993
- Fan Y, Ma W, Han D, Gan S, Dong X, Niu L (2015) Convenient recycling of 3D AgX/graphene aerogels (X = Br, Cl) for efficient photocatalytic degradation of water pollutants. *Adv Mater* 27:3767–3773
- Li J, Stling M (2013) Prevention of graphene restacking for performance boost of supercapacitors—a review. *Crystals* 3:163

12. Pisal AA, Rao AV (2016) Development of hydrophobic and optically transparent monolithic silica aerogels for window panel applications. *J Porous Mater* 24:1–11
13. Schwertfeger F, Hüsing N, Schubert U (1994) Influence of the nature of organic groups on the properties of organically modified silica aerogels. *J Sol-Gel Sci Technol* 2:103–108
14. Hüsing N, Schubert U (1997) Organofunctional silica aerogels. *J Sol-Gel Sci Technol* 8:807–812
15. Li CC, Cheng XD, Li Z, Pan YL, Huang YJ, Gong LL (2017) Mechanical, thermal and flammability properties of glass fiber film/silica aerogel composites. *J Non-Cryst Solids* 457:52–59
16. Karout A, Buisson P, Perrard A, Pierre AC (2005) Shaping and mechanical reinforcement of silica aerogel biocatalysts with ceramic fiber felts. *J Sol-Gel Sci Technol* 36:163–171
17. Wang J (1995) Monolithic silica aerogel insulation doped with TiO₂ powder and ceramic fibers. *J Non-Cryst Solids* 186:296–300
18. Xu L, Jiang Y, Feng J, Yue C (2015) Infrared-opacified Al₂O₃–SiO₂ aerogel composites reinforced by SiC-coated mullite fibers for thermal insulations. *Ceram Int* 41:437–442
19. Kim CY, Lee JK, Kim BI (2008) Synthesis and pore analysis of aerogel–glass fiber composites by ambient drying method. *Colloid Surf A* 313:179–182
20. Li Z, Cheng XD, He S, Shi XJ, Gong LL, Zhang HP (2016) Aramid fibers reinforced silica aerogel composites with low thermal conductivity and improved mechanical performance. *Compos Part A Appl Sci Manuf* 99:349–355
21. Liu HL, Chu P, Li HY, Zhang HY, Li JD (2016) Novel three-dimensional halloysite nanotubes/silica composite aerogels with enhanced mechanical strength and low thermal conductivity prepared at ambient pressure. *J Sol-Gel Sci Technol* 80:651–659
22. Leventis N (2007) Three-dimensional core–shell superstructures: mechanically strong aerogels. *Acc Chem Res* 40:874–884
23. Yang XG, Wei J, Shi DQ, Sun YT, Lv SQ, Feng J, Jiang YG (2014) Comparative investigation of creep behavior of ceramic fiber-reinforced alumina and silica aerogel. *Mater Sci Eng R* 609:125–130
24. Yuan B, Ding S, Wang D, Li H (2012) Heat insulation properties of silica aerogel/glass fiber composites fabricated by press forming. *Mater Lett* 75:204–206
25. Huang Y, Liu JL (2015) Energy and visual performance of the silica aerogel glazing system in commercial buildings of Hong Kong. *Constr Build Mater* 94:57–72
26. Zhang Y, Jing OY, Yang HM (2014) Metal oxide nanoparticles deposited onto carbon-coated halloysite nanotubes. *Appl Clay Sci* 95:252–259
27. Tayser SG, Abdul AHK, Patina KAM, Ahmed AA, Abu BS, Mohamed HN, Ahed HJ (2017) Unique halloysite nanotubes–polyvinyl alcohol–polyvinylpyrrolidone composite complemented with physico-chemical characterization. *Polymers (Basel)* 9:207
28. Cheng ZL, Qin XX, Liu Z, Qin DZ (2017) Electrospinning preparation and mechanical properties of PVA/HNTs composite nanofibers. *Polym Adv Technol* 28:52–56
29. Yuan P, Tan D, Annabi-Bergaya F (2015) Properties and applications of halloysite nanotubes: recent research advances and future prospects. *Appl Clay Sci* 112:75–93
30. Gaaz TS, Sulong AB, Kadhum AAH, Al-Amiery AA, Nassir MH, Jaaz AH (2017) The impact of halloysite on the thermo-mechanical properties of polymer composites. *Molecules* 22:838
31. Lvov Y, Wang WC, Zhang LQ, Fakhrullin R (2016) Halloysite clay nanotubes for loading and sustained release of functional compounds. *Adv Mater* 28:227–1250
32. Lvov Y, Abdullayev E (2013) Functional polymer–clay nanotube composites with sustained release of chemical agents. *Prog Polym Sci* 38:1690–1719
33. Liu M, Guo B, Du M, Chen F, Jia D (2009) Halloysite nanotubes as a novel β -nucleating agent for isotactic polypropylene. *Polymer* 50:3022–3030
34. Rooj S, Das A, Thakur V, Mahaling RN, Bhowmick AK, Heinrich G (2010) Preparation and properties of natural nanocomposites based on natural rubber and naturally occurring halloysite nanotubes. *Mater Des* 31:2151–2156
35. Kamble R, Ghag M, Gaikwad S, Panda BK (2012) Halloysite nanotubes and applications: a review. *J Adv Sci Res* 3:25–29
36. Zhang AB, Pan L, Zhang HY, Liu ST, Ye Y, Xia MS, Chen XG (2012) Effects of acid treatment on the physico-chemical and pore characteristics of halloysite. *Colloid Surf A* 396:182–188
37. Cavallaro G, Donato DI, Lazzara G, Milioto S (2011) Films of halloysite nanotubes sandwiched between two layers of biopolymer: from the morphology to the dielectric, thermal, transparency, and wettability properties. *J Phys Chem C* 115:20491–20498
38. Cavallaro G, Lazzara G, Milioto S (2010) Dispersions of nanoclays of different shapes into aqueous and solid biopolymeric matrices. Extended physicochemical study. *Langmuir* 27:1158–1167
39. Ferris CJ, Gilmore KJ, Wallace GG, Panhuis MIH (2013) Modified gellan gum hydrogels for tissue engineering applications. *Soft Matter* 9:3705–3711
40. Vahedi V, Pasbakhsh P, Chai SP (2015) Toward high performance epoxy/halloysite nanocomposites: new insights based on rheological, curing, and impact properties. *Mater Des* 68:42–53
41. Peng WH, Lee YY, Wu C, Wu KCW (2012) Acid–base bifunctionalized, large-pored mesoporous silica nanoparticles for cooperative catalysis of one-pot cellulose-to-HMF conversion. *J Mater Chem* 22:23181–23185
42. Zeng S, Reyes C, Liu J, Rodgers PA, Wentworth SH, Sun L (2014) Facile hydroxylation of halloysite nanotubes for epoxy nanocomposite applications. *Polymer* 55:6519–6528
43. Lee IW, Li J, Chen X, Park HJ (2015) Electrospun poly(vinyl alcohol) composite nanofibers with halloysite nanotubes for the sustained release of sodium d-pantothenate. *J Appl Polym Sci* 133:4
44. Liu HL, He X, Li HY, Yang AW, Xiao R, Wei N (2017) Preparation and properties of HNTs/SiO₂ composite aerogels. *J Synth Cryst* 46:2277–2282
45. Cai J, Liu SL, Feng J, Kimura S (2012) Cellulose-silica nanocomposite aerogels by in situ formation of silica in cellulose gel. *Angew Chem Int Ed* 51:2076–2079
46. Sai H, Xing L, Xiang J, Cui L (2013) Flexible aerogels based on an interpenetrating network of bacterial cellulose and silica by a non-supercritical drying process. *J Mater Chem A* 1:7963–7970
47. Fei ZF, Yang ZC, Chen GB, Li KF, Zhao S, Su GH (2018) Preparation and characterization of glass fiber/polyimide/SiO₂ composite aerogels with high specific surface area. *J Mater Sci*. <https://doi.org/10.1007/s10853-018-2553-4>
48. Alaoui AH, Woignier T, Scherer GW, Phalippou J (2008) Comparison between flexural and uniaxial compression tests to measure the elastic modulus of silica aerogel. *J Non-Cryst Solids* 354:4556–4561
49. He C, He YL, Xie T, Liu Q (2013) Predictions of the effective thermal conductivity for aerogel-fiber composite insulation materials using lattice Boltzmann method. *J Eng Thermophys* 34:742–745
50. Qu ZG, Fu YD, Liu Y, Zhou L (2018) Approach for predicting effective thermal conductivity of aerogel materials through a modified lattice Boltzmann method. *Appl Therm Eng* 132:730–739
51. Lepinasse E, Goetz V, Crosat G (1994) Modelling and experimental investigation of a new type of thermochemical transformer based on the coupling of two solid–gas reactions. *Chem Eng Process* 33:125–134